Mesoporous Materials

DOI: 10.1002/ange.201306004

Crystallization of Tungsten Trioxide Having Small Mesopores: Highly Efficient Photoanode for Visible-Light-Driven Water Oxidation**

*Debraj Chandra, Kenji Saito, Tatsuto Yui, and Masayuki Yagi**

Recent developments of nanostructured materials have widened their application in photoelectrochemical (PEC) water splitting for direct conversion of solar energy into green and storable hydrogen fuel.[1–4] Water oxidation is considered to be the energy-demanding bottleneck in PEC solar fuel devices and thus related photoanode materials have been extensively studied.[5–8] Tungsten trioxide (WO_3) has attracted immense attention as a photoanode material in PEC devices because of its visible-light response (band gap, $E_g = 2.6$–2.8 eV), a favorable valance band edge position for O_2 evolution (3 V versus the normal hydrogen electrode, NHE), and good photochemical stability.[9–13] So far, the mesoporous architectures of photoanodes are promising for applications in solar energy conversion.[13–16] A system having organized small mesopores[17–19] (pore diameter, about 2–3 nm) can offer 1) a large internal surface area; and 2) a shorter solid-state carrier diffusion length in the nanosized wall (< 10 nm; Scheme 1 a); owing to their smaller void spaces inside pores and slimmer pore walls relative to conventional (pore diameter, about 5–10 nm) and interparticle (particles spacing, > 15 nm) mesoporous systems. However, particularly in case of WO_3 high crystallinity is needed for a PEC performance as a photoanode.[10,20] Optimum thermal crystallization of a system having small mesopores is still unachieved because mesoporous structures surrounded by slim pore walls collapsed during thermal treatment because of undesirable growth of crystallites.[17,21] Therefore, only interparticle mesoporous systems of WO_3 photoanodes have been exploited in PEC water splitting so far.[10,12,13]

In surfactant-templated mesoporous systems (> 5 nm pores),[22,23] thermal crystallization was attributively reported for TiO_2[24–26] and was rarely described for other semiconductors.[27,28] Regarding mesoporous WO_3, most of the studies are associated with either amorphous or poorly crystallized frameworks,[29–32] except for the high-temperature crystallization of a system having large mesopores (> 10 nm), reported by Smarsly and co-workers.[28] High-temperature crystallization was also demonstrated by providing amorphous carbon support inside mesopores (about 5–10 nm) for block-copolymer-templated TiO_2[26] and Nb-Ta-mixed oxide,[27] which involve either strong acidic conditions[26] or multistep polymerization processes.[27] In systems having small mesopores such harsh conditions could cause severe degradation of porous structures, composed of highly susceptible slim pore walls. We have focused on an organic amphiphilic molecule, 2-(hexadecylaminomethyl)pyridine (PAL2-16)[17–19] which can provide carbon support inside pores on simple thermal carbonization even at high temperature in N_2. Herein, we report the first successful thermal crystallization in a newly developed WO_3 system having organized small mesopores (about 2–3 nm) by employing a simple one-step procedure of an in situ surfactant-thermal-carbonization method using PAL2-16 (Scheme 1 b). The small mesopores are shown to improve the performance of the PEC water oxidation.

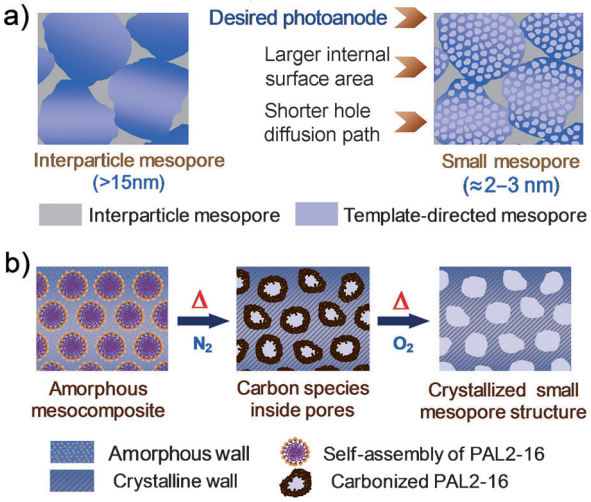

Scheme 1. a) Advantages of small mesopores in the WO_3 photoanode relative to a conventional interparticle mesoporous configuration. b) Conceptual scheme for the crystallization of WO_3 having small mesopores by an in situ surfactant-thermal-carbonization method.

The synthesis is based on condensation/dissociation of anionic peroxo-tungstic acid (PA) precursors to amorphous WO_3 around protonated self-assembly of PAL2-16 in ethanol. According to the in situ surfactant-thermal-carbonization method, amorphous WO_3/PAL2-16 composite was first simultaneously carbonized and crystallized in N_2 at 450–550 °C (Scheme 1 b). Carbon was burned out by switching N_2 to O_2 atmosphere at the corresponding crystallization temperature and the resulting crystalline sample was denoted as "mesoporous WO_3" based on the later characterization. The control

[*] Dr. D. Chandra, Prof. K. Saito, Prof. T. Yui, Prof. M. Yagi
Department of Materials Science and Technology
Faculty of Engineering, Niigata University
8050 Ikarashi-2, Niigata 950-2181 (Japan)
E-mail: yagi@eng.niigata-u.ac.jp
Prof. M. Yagi
Precursory Research for Embryonic Science (PRESTO)
Science and Technology Agency (JST)
4-1-8 Honcho, Kawaguchi, Saitama 332-0012 (Japan)

[**] This work is financially supported by a grant-in-aid for scientific research from the JSPS. D.C. thanks JSPS for providing a postdoctoral fellowship.

Supporting information for this article is available on the WWW under http://dx.doi.org/10.1002/anie.201306004.

samples were prepared by direct crystallization of WO_3/PAL2-16 in air and without PAL2-16 (denoted as "interparticle WO_3" and "bulk WO_3", respectively).

The transmission electron microscopic (TEM) image of the amorphous WO_3/PAL2-16 composite (Figure 1a) shows a well-defined and highly ordered 2D hexagonal mesostructures (space group *P6mm*) with a pore diameter of about 3 nm over a large domain. Crystallization at 450 °C by the in situ surfactant-thermal-carbonization method led to deformation of the 2D hexagonal mesostructures with only short-range ordering (Figure 1b) which could be traced back to the formation of dense nanocrystals in pore walls. During crystallization at 550 °C (Figure 1c), complete transformation of the ordered mesostructure to the disordered phase was observed possibly because of an increased size of the nanocrystals. Small angle X-ray diffraction (XRD) patterns (see Figure S1 in the Supporting Information) also shows that four reflections of a 2D hexagonal WO_3/PAL2-16 mesocomposite have transformed into a single peak of the disordered mesophase after crystallization, which is consistent with TEM observations. A representative high-resolution TEM (HRTEM) image (Figure 2a) of mesoporous WO_3 (550 °C) revealed that the slim pore walls were composed of randomly oriented tiny crystalline particles of an estimated size in the range of 4–6 nm. Selected-area electron diffraction (SAED) patterns of the same mesostructure (Figure 2b) show several well-resolved diffraction rings and many diffraction spots suggesting polycrystalline nanocrystals. The *d*-spacings calculated from SAED patterns were in good agreement with phase-pure monoclinic WO_3 (JCPDS number: 43-1305), which is also supported by the wide-angle XRD patterns (Figure S1). The retention of the mesostructure at high crystallization temperature (550 °C) is ascribable to the in situ surfactant-thermal-carbonization process, because TEM images of WO_3/PAL2-16 after direct crystallization in air at 450 °C (Figure S2) show the complete collapse of the small mesopores and the existence of only large interparticle mesopores between rigid crystalline WO_3 particles. (No peak is detectable in the small-angle XRD pattern shown in Figure S1.)

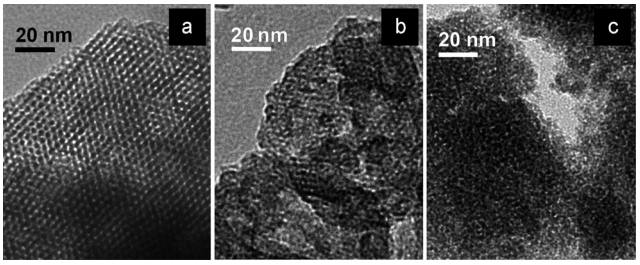

Figure 1. TEM images of the mesoporus WO_3 samples for a) amorphous WO_3/PAL2-16 composite and b,c) after being crystallized by an in situ surfactant-thermal-carbonization method at b) 450 and c) 550 °C.

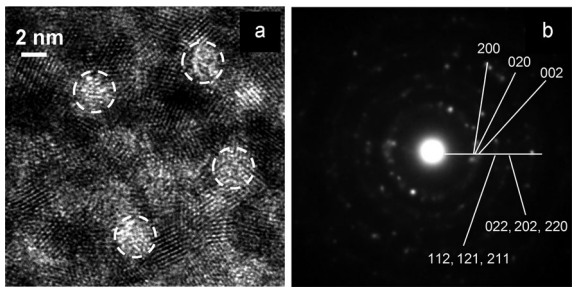

Figure 2. a) HRTEM image and b) SAED pattern of crystallized mesoporous WO_3 at 550 °C. In the HRTEM image a few pores are highlighted by white circles.

N_2 sorption isotherms of WO_3 samples prepared by the in situ surfactant-thermal-carbonization method (Figure 3a and b) show type-IV characteristics (up to a relative pressure, $P/P_0 \approx 0.75$) of uniform mesoporous materials.[33,34] N_2 uptake of the mesopores through a capillary condensation step started at $P/P_0 \approx 0.2$. Another sharp N_2 uptake around $P/P_0 >$ 0.75 indicates secondary interparticle porosity. H2-type hysteresis loops may be related to the roughness of the pores and particle surfaces.[35] The pore size distributions studied by the Barrett-Joyner-Halenda (BJH) method show bimodal porosity, arising from template-directed mesopores of about 2.5 nm and interparticle mesopores of >15 nm (Table S1). Scanning electron microscopic (SEM) images in Figure S3 indicate that the interparticle mesopores originate from the void space between WO_3 particles. BET surface areas of mesoporous WO_3 samples are exceptionally high, that is, 197 and 158 $m^2 g^{-1}$ at 450 and 550 °C, respectively. Direct crystallization of amorphous WO_3/PAL2-16 in air at 450 °C (Figure 3c) shows only interparticle mesopores of about 25 nm and a drastically reduced BET surface area (31 $m^2 g^{-1}$). The bulk WO_3 sample (Figure 3d) exhibits a very low BET surface area (9 $m^2 g^{-1}$) and large interparticle pores of about 50 nm. Considering the high density of crystalline WO_3 (7.16 $g cm^{-3}$), the BET surface area of our WO_3 having small mesopores is comparable with ordered mesoporous silica[33,34] and to the best of our knowledge about two times higher compared to any other mesoporous WO_3 material reported so far.[28–32]

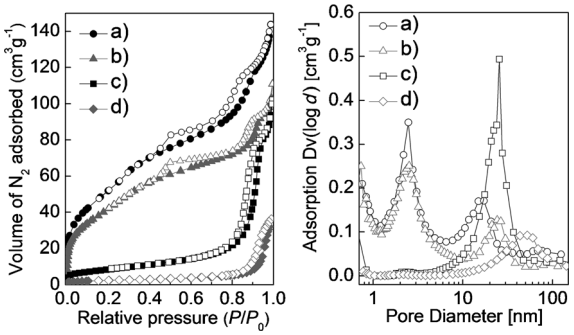

Figure 3. N_2 sorption isotherms (left) and pore size distributions (right) of mesoporous WO_3 samples crystallized by an in situ surfactant-thermal-carbonization method at a) 450 °C and b) 550 °C, and c) interparticle WO_3 crystallized in air at 450 °C. d) Bulk WO_3 crystallized under identical conditions of (a) at 450 °C.

Raman spectra (Figure S4) of mesoporous WO_3 crystallized at 550 °C in N_2 exhibits two broad bands for amorphous carbon[36] around 1365 and 1590 cm^{-1} which completely disappeared after calcination in O_2. Thermogravimetric (TG) analysis started with the amorphous WO_3/PAL2-16 composite (Figure S5) shows almost 16 and 32% weight loss in N_2 and air, respectively, at 550 °C. These results indicate that a significant amount of carbon was contained inside the pores during crystallization in N_2. Furthermore, the N_2 sorption isotherm (Figure S6) of the crystallized mesoporous WO_3 at 550 °C before carbon removal shows the much lower BET surface area (64 $m^2 g^{-1}$) and the smaller pore size (2.2 nm) compared to the final mesoporous WO_3, implying that carbonaceous species are located around the mesoporous channel to form a tubular-like layer (Scheme 1 B). The inner carbon layer could act as a protective support to prohibit the undesired WO_3 crystallite growth by offsetting the developed tensile stress during crystallization. The resultant crystalline mesostructure is well-retained after removal of carbon.

The mesoporous WO_3 films were prepared on a fluorine doped tin oxide (FTO) electrode using a simple squeeze technique, and the film thickness was measured to be about 7 μm by cross-sectional SEM observations (Figure S3). Figure 4 shows action spectra of the incident photon-to-current conversion efficiency (IPCE) at 0.5 V versus Ag/AgCl

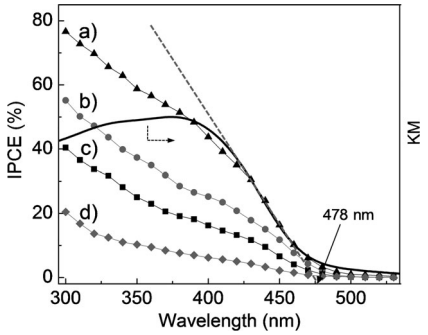

Figure 4. Action spectra of IPCE plots of photoanodes based on mesoporous WO_3 crystallized at a) 550 °C and b) 450 °C, c) interparticle WO_3 crystalized at 550 °C, and d) bulk WO_3 crystallized at 550 °C, as measured in a 0.1 M phosphate buffer solution (pH of about 6.0) at 0.5 V versus Ag/AgCl. The black solid line shows UV/Vis diffuse reflectance spectra as Kubelka-Munk (KM) function of mesoporous WO_3 crystallized at 550 °C.

using different FTO/WO_3 photoanodes. The photocurrent was generated below 480 nm for all the electrodes used, which agrees with a band gap energy of 2.59 eV (478 nm), estimated from the diffuse reflectance spectrum of the mesoporous WO_3 film (Figure 4). This indicates that the photocurrent is generated by the band gap excitation of the WO_3. At the crystallization temperature of 550 °C, IPCE at 420 nm of mesoporous WO_3 (35%) (Figure 4 a) is about three- and seven-times higher compared to that of interparticle WO_3 (13%; Figure 4 c) and bulk WO_3 (5%; Figure 4 d), respectively. Mesoporous WO_3 crystallized at 450 °C shows markedly low IPCE (21%; Figure 4 b) at 420 nm in contrast to its highest surface area (197 $m^2 g^{-1}$) observed from N_2 sorption analysis. The result signifies the importance of high crystallinity in mesoporous WO_3 at 550 °C without any considerable depletion of surface physical properties for the high IPCE.

Photoelectrocatalysis over different FTO/WO_3 electrodes was conducted in a 0.1 M phosphate buffer solution (pH ≈ 6.0) under potentiostatic conditions at 0.5 V versus Ag/AgCl for 1 h, upon visible light irradiation ($\lambda > 420$ nm). The photocurrent–time profile of mesoporous WO_3 (Figure 5 b) gave

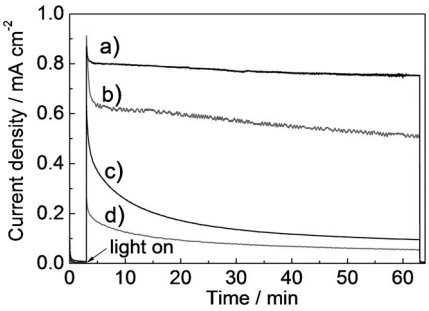

Figure 5. Photocurrent density versus time profiles of WO_3 electrodes crystallized at 550 °C for a,b) mesoporous WO_3 c) interparticle WO_3, and d) bulk WO_3 in (a) the presence and (b–d) the absence of Co^{2+} ions in a 0.1 M phosphate buffer solution (pH of about 6.0) at 0.5 V versus Ag/AgCl.

0.66 mA cm^{-2} of photocurrent at 1 minute, decreased to 0.50 mA cm^{-2} after 1 h (about 24% decrease). Relatively lower initial photocurrent at 1 minute was observed for interparticle WO_3 (0.42 mA cm^{-2}; Figure 5 c) and bulk WO_3 (0.19 mA cm^{-2}; Figure 5 d), which is consistent with cyclic voltammetry (CV) data (Figure S7). Moreover, the photocurrent decayed much rapidly for interparticle (about 78%) and bulk (about 70%) WO_3 photoanodes after 1 h of illumination. The charge amount passed during 1 h photoelectrocatalysis for mesoporous WO_3 (2.05 C) is 3.5 and 6.6 times higher than those of interparticle WO_3 (0.58 C) and bulk WO_3 (0.31 C), respectively (Table S2). As a consequence of the high charge amount, mesoporous WO_3 evolved the markedly higher amount of O_2 (4.21 μmol) compared to the interparticle WO_3 (0.93 μmol) and bulk WO_3 (0.35 μmol; Table S2). Faradaic efficiency of O_2 evolution (FE_{O_2}) for mesoporous WO_3 (about 79%) is also much higher than their interparticle (about 61%) and bulk (about 44%) counterparts.

High PEC water oxidation performance of the mesoporous WO_3 photoanode (crystallized at 550 °C) is ascribed to both the high surface area (158 $m^2 g^{-1}$) which offers a large number of oxidation sites at the electrolyte–WO_3 interface, and the shorter carrier diffusion length in the nanosized pore walls (about 4–6 nm) which increases the possibility of photogenerated holes to take part in the oxidation of water prior to recombination. The high photostability and FE_{O_2} for mesoporous WO_3 could arise from the less oxidized WO_3 surface during photoelectrocatalysis. The slow kinetics of the water oxidation results in hole accumulation at the surface, and subsequent photo-oxidation of WO_3 by holes to form inactive tungsten-peroxo adducts.[11] The higher surface-to-

mass ratio of mesoporous WO_3 could decrease the effective concentration of accumulated holes at the surface and suppress the formation of the unfavorable peroxide adducts. This proposed mechanism is supported by the enhancement of the water oxidation activity by Co^{2+} ions in the electrolyte solution (Figure 5a). (Recent studies show that Co^{2+} ions in an electrolyte solution enhance the photoelectrocatalytic water oxidation activity at a hematite photoanode.[37]) In the presence of 0.1 mM Co^{2+} ions in the phosphate buffer solution, mesoporous WO_3 shows a high initial photocurrent (0.80 mA cm^{-2} at 1 minute) and preservation of about 95% of the photocurrent after 1 h of photoelectrocatalysis. The amount of O_2 evolution (5.84 μmol, FE_{O_2} 81%, 2.79 C of charge passed; Table S2) was 1.4 times higher compared to the absence of Co^{2+} ions. The similar enhancement by Co^{2+} ions was also observed in a Na_2SO_4 solution (pH of about 6.0; Figure S8), suggesting that the enhancement by the Co-Pi catalyst[38] formed on the WO_3 surface is unlikely during photoelectrocatalysis. Energy dispersive X-ray spectroscopic data did not show evidence of CoO_x catalysts[39] deposited on the surface after photoelectrocatalysis. These results suggest that the enhancement by addition of Co^{2+} ions is ascribed to acceleration of the water oxidation reaction at the WO_3 surface by Co^{2+} ions in the electrolyte solution, which significantly suppress the formation of peroxide adducts. The mesoporous WO_3 photoanode is promising for high-performance solar energy conversion, and moreover the essence of our fabrication approach is expected to be widely applicable in advancement of other unattained crystalline architectures having small mesopores for other applications.

Received: July 10, 2013
Published online: October 7, 2013

Keywords: crystal engineering · mesoporous materials · water oxidation · photoelectrocatalysis · tungsten

[1] M. Grätzel, *Nature* **2001**, *414*, 338 – 344.
[2] P. V. Kamat, K. Tvrdy, D. R. Baker, J. G. Radich, *Chem. Rev.* **2010**, *110*, 6664 – 6688.
[3] S. Dahl, I. Chorkendorff, *Nat. Mater.* **2012**, *11*, 100 – 101.
[4] Y. Li, Z.-Y. Fu, B.-L. Su, *Adv. Funct. Mater.* **2012**, *22*, 4634 – 4667.
[5] H. G. Kim, P. H. Borse, J. S. Jang, C. W. Ahn, E. D. Jeong, J. S. Lee, *Adv. Mater.* **2011**, *23*, 2088 – 2092.
[6] K. Maeda, K. Domen, *Angew. Chem.* **2012**, *124*, 10003 – 10007; *Angew. Chem. Int. Ed.* **2012**, *51*, 9865 – 9869.
[7] T. Hisatomi, H. Dotan, M. Stefik, K. Sivula, A. Rothschild, M. Grätzel, N. Mathews, *Adv. Mater.* **2012**, *24*, 2699 – 2702.
[8] Y. Li, T. Takata, D. Cha, K. Takanabe, T. Minegishi, J. Kubota, K. Domen, *Adv. Mater.* **2013**, *25*, 125 – 131.
[9] X. Chen, J. Ye, S. Ouyang, T. Kako, Z. Li, Z. Zou, *ACS Nano* **2011**, *5*, 4310 – 4318.
[10] B. Yang, Y. Zhang, E. Drabarek, P. R. F. Barnes, V. Luca, *Chem. Mater.* **2007**, *19*, 5664 – 5672.
[11] J. A. Seabold, K.-S. Choi, *Chem. Mater.* **2011**, *23*, 1105 – 1112.
[12] F. M. Pesci, A. J. Cowan, B. D. Alexander, J. R. Durrant, D. R. Klug, *J. Phys. Chem. Lett.* **2011**, *2*, 1900 – 1903.
[13] J. K. Kim, K. Shin, S. M. Cho, T.-W. Lee, J. H. Park, *Energy Environ. Sci.* **2011**, *4*, 1465 – 1470.
[14] M. Kato, T. Cardona, A. W. Rutherford, E. Reisner, *J. Am. Chem. Soc.* **2012**, *134*, 8332 – 8335.
[15] J. Kim, J. K. Koh, B. Kim, J. H. Kim, E. Kim, *Angew. Chem.* **2012**, *124*, 6970 – 6975; *Angew. Chem. Int. Ed.* **2012**, *51*, 6864 – 6869.
[16] M. Zukalová, A. Zukal, L. Kavan, M. K. Nazeeruddin, P. Liska, M. Grätzel, *Nano Lett.* **2005**, *5*, 1789 – 1792.
[17] D. Chandra, T. Ohji, K. Kato, T. Kimura, *Langmuir* **2011**, *27*, 11436 – 11443.
[18] D. Chandra, S. Mridha, D. Basak, A. Bhaumik, *Chem. Commun.* **2009**, 2384 – 2386.
[19] D. Chandra, N. Mukherjee, A. Mondal, A. Bhaumik, *J. Phys. Chem. C* **2008**, *112*, 8668 – 8674.
[20] C. Santato, M. Odziemkowski, M. Ulmann, J. Augustynski, *J. Am. Chem. Soc.* **2001**, *123*, 10639 – 10649.
[21] H. Shibata, T. Ogura, T. Mukai, T. Ohkubo, H. Sakai, M. Abe, *J. Am. Chem. Soc.* **2005**, *127*, 16396 – 16397.
[22] C. Sanchez, C. Boissière, D. Grosso, C. Laberty, L. Nicole, *Chem. Mater.* **2008**, *20*, 682 – 737.
[23] P. Yang, D. Zhao, D. I. Margolese, B. F. Chmelka, G. D. Stucky, *Chem. Mater.* **1999**, *11*, 2813 – 2826.
[24] J. D. Bass, D. Grosso, C. Boissiere, C. Sanchez, *J. Am. Chem. Soc.* **2008**, *130*, 7882 – 7897.
[25] W. Zhou, F. Sun, K. Pan, G. Tian, B. Jiang, Z. Ren, C. Tian, H. Fu, *Adv. Funct. Mater.* **2011**, *21*, 1922 – 1930.
[26] R. Zhang, B. To, D. Zhao, *Chem. Eur. J.* **2010**, *16*, 9977 – 9981.
[27] T. Katou, B. Lee, D. Lu, J. N. Kondo, M, Hara, K. Domen, *Angew. Chem.* **2003**, *115*, 2484 – 2487; *Angew. Chem. Int. Ed.* **2003**, *42*, 2382 – 2385.
[28] T. Brezesinski, D. Fattakhova-Rohlfing, S. Sallard, M. Antonietti, B. M. Smarsly, *Small* **2006**, *2*, 1203 – 1211.
[29] L. M. Bertus, A. Dutta, *Ceram. Int.* **2012**, *38*, 2873 – 2882.
[30] S.-H. Baeck, K.-S. Choi, T. F. Jaramillo, G. D. Stucky, E. W. McFarland, *Adv. Mater.* **2003**, *15*, 1269 – 1273.
[31] W. Wang, Y. Pang, S. N. B. Hodgson, *J. Sol-Gel Sci. Technol.* **2010**, *54*, 19 – 28.
[32] P. Yang, D. Zhao, D. I. Margolese, B. F. Chmelka, G. D. Stucky, *Nature* **1998**, *396*, 152 – 155.
[33] C. T. Kresge, M. E. Leonowicz, W. J. Roth, J. C. Vartuli, J. S. Beck, *Nature* **1992**, *359*, 710 – 712.
[34] D. Chandra, T. Yokoi, T. Tatsumi, A. Bhaumik, *Chem. Mater.* **2007**, *19*, 5347 – 5354.
[35] A. Grosman, C. Camille, *Langmuir* **2008**, *24*, 3977 – 3986.
[36] A. C. Ferrari, J. Robertson, *Phys. Rev. B* **2000**, *61*, 14095 – 14107.
[37] A. Kay, I. Cesar, M. Grätzel, *J. Am. Chem. Soc.* **2006**, *128*, 15714 – 15721.
[38] M. W. Kanan, D. G. Nocera, *Science* **2008**, *321*, 1072 – 1075.
[39] M. Higashi, K. Domen, R. Abe, *J. Am. Chem. Soc.* **2013**, *135*, 10238 – 10241.

